Transient response of the Delft jet-in-hot coflow flames

Ernst Oldenhof, Mark J. Tummers *, Eric H. van Veen, Dirk J.E.M. Roekaerts

Department of Multi-Scale Physics, Delft University of Technology, Lorentzweg 1, 2628 CJ Delft, The Netherlands

ABSTRACT

The ignition of impulsively started jets of natural gas in a hot coflow has been studied, with the aim of gaining insight into the processes that occur in a furnace equipped with regenerative burners. The development of the velocity field was measured in a time resolved manner with Laser Doppler Anemometry (LDA) and Particle Image Velocimetry (PIV) at 10 kHz. Furthermore, simultaneous PIV and Planar Laser Induced Fluorescence of the OH-radical (OH-PLIF) were employed in combination with high-speed recordings of flame luminescence to map the ignition sequence. A characteristic feature of the impulsively started jets was that the turbulent phase was preceded by a laminar phase, during which no significant amount of combustion took place. After the sudden transition towards a turbulent state, significant ignition delay times were observed. As demonstrated in earlier work Oldenhof et al. (2011) [1], the radial temperature gradient of the coflow makes the entrainment of coflow fluid into the jet region very important to the jet stabilisation, influencing strongly the lift-off height. Using the time-resolved PIV data, the transport of fluid parcels in the coflow region was monitored during the transition towards the turbulent state. This transport is governed by the low velocities of the coflow and as a result, ignition delay times and the time until a steady state of combustion is attained are not solely related to jet time scales. It is thus concluded that in the presence of large-scale inhomogeneities, ignition delay times are several times greater than the time needed for the velocity field of the jet to reach its steady turbulent state.

© 2011 The Combustion Institute. Published by Elsevier Inc. All rights reserved.

1. Introduction

Recycling of flue gas heat is a prominent feature of flameless combustion. Rather than having the heat escape from the furnace along with the flue gases, the heat is used to preheat one or both reactant streams [2]. This preheating can be achieved by a recuperative system which operates by continuously exchanging heat between outgoing and ingoing flows. A more efficient solution is offered by a regenerative system, characterised by two alternating configurations [3]. During the first part of the regenerative cycle, one set of burners supplies reactants to the furnace and the other set of burners acts as flue gas exhausts. Regenerators in the exit burners (for instance ceramic honeycombs) extract heat from the exhaust gases, while regenerators in the supplying set of burners feed the previously extracted heat to the reactant stream. In the second part of the cycle, the roles are reversed. This complete cycle has a period of typically 20 s, introducing an inherent unsteadiness in the furnace. Since the flow field can change as frequent as once in every 10 s, transient phenomena could be of significance for the combustion process as a whole.

Whereas experimental and numerical studies of transient processes in engines are common practise [4,5], transient phenomena in regenerative furnaces in flameless mode have not yet been addressed in detail. The lack of optical accessibility of large setups prohibits the use of laser diagnostics and measured quantities are usually not well resolved in space or time. Detailed data on transient processes in a furnace are therefore simply unavailable. The simplified case of a transient jet in a hot, unconfined coflow is much easier to study experimentally. Nevertheless, studies on transient behaviour of such flames are also sparse in literature.

Non-reacting transient turbulent jets have been studied more extensively, a summary is provided by Joshi and Schreiber [6]. An important result is the square root dependence of the jet penetration with time [7]. Atassi et al. [8] showed that a sudden decrease in the exit velocity of a turbulent jet leads to disturbances on the centreline at large axial distances with a duration of the order of the local time scale (determined by the local jet diameter and centreline velocity). Cossali et al. [9] examined the evolution of the entrainment of an impulsively started turbulent jet in its near field ($z/D < 22$), with D the nozzle diameter. The centreline velocity was seen to evolve faster than the entrainment flux, which took about 7 ms to reach the steady state within the considered domain. When normalised, this corresponds to about 180 jet time scales (the nozzle diameter divided by the jet velocity).

In the context of ignition in Diesel-like conditions, Naber et al. [10] investigated the influence of fuel composition on ignition delays of autoignition and found that the presence of higher

---

* Corresponding author. Fax: +31 15 27 81204.
 *E-mail address:* M.J.Tummers@tudelft.nl (M.J. Tummers).

alkanes strongly influenced ignition delay times. More recently, Fast et al. [11] carried out a comprehensive study on ignition of dimethyl ether (DME) jets injected into a high-pressure vessel containing nearly stagnant heated air. The development of the mixture fraction field, the velocity at the nozzle exit and heat generation (by means of high-speed Schlieren imaging) was recorded, relative to time of injection. This phase-resolved data revealed a two-stage ignition sequence. The first stage was characterised by a moderate temperature increase over a large spatial extent, followed by a second stage of more intense heat release, after which a non-premixed flame was formed. Ignition delay times were found to be largely unaffected by variations in jet velocity, and mainly dependent on chemical kinetics.

In this work, the ignition behaviour of transient jets is studied in the Delft jet-in-hot-coflow (DJHC) burner. This setup was designed to study turbulence-chemistry interaction in circumstances resembling those found in flameless combustion. Two important characteristics of the flames produced by the DJHC-burner are the random ignition phenomena that stabilise the flame [12] and the role of entrainment of the non-homogeneous coflow into the flame zone [1]. The main objective of the present study is to get insight into the processes that occur when the fuel jet is suddenly started, and their relation to the ignition delay.

2. Experimental setup

2.1. Burner and fuel injection mechanism

The DJHC burner consists of a partially premixed ring burner, enclosed in a stainless steel tube with an outer diameter of 89.2 mm, that generates a coflow of hot flue gases. This coflow surrounds a cooled fuel jet that emerges from a stainless steel tube of 4.5 mm inner diameter, as illustrated in the inset of Fig. 1. The burner was designed to mimic conditions found in flameless combustion. Due to the radiative and convective cooling of the outer burner tube, the flue gases carry a heat loss, reducing the adiabatic flame temperature. The design is based on that of the Adelaide jet-in-hot coflow burner [13]. More details on the geometry can be found in [1].
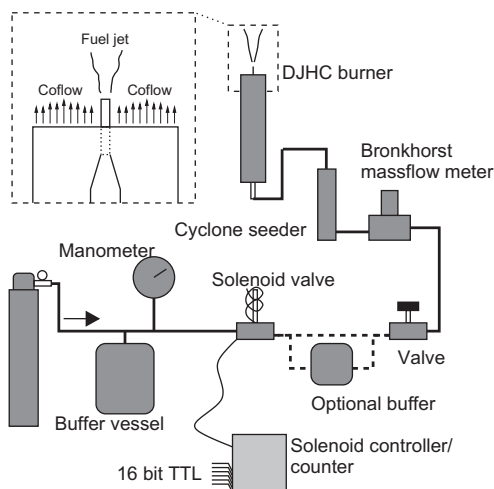
Fig. 1. Fuel injection system. The fuel enters the system at the arrow at a fixed pressure (of either 0.4 bar or 1.0 bar). The 4 l buffer vessel ensures that the pressure fluctuations due to the periodic opening of the solenoid valve are small. The solenoid valve is operated by a digital controller that also generates a 16-bit TTL timer signal to be used by the measurement devices. Before entering the DJHC-burner, the fuel flow is seeded by a cyclone seeder. Optionally, a small buffer can be used to decrease the rate of velocity increase of the jet (used for the "slow" case).

To generate reproducible transient jets, the burner was retrofitted with an electrically pulsed fuel injection system, connected to a digital timing system. The fuel used in the jet stream is a synthetic mixture of 80% methane, 5% ethane and 15% nitrogen, thus resembling Dutch natural gas. Special care was taken to design a system that generates a fast and highly reproducible injection of fuel. The system is outlined in Fig. 1. A solenoid valve was installed downstream of a buffer vessel with a volume of 4 l, which serves to minimise pressure drop during the jet pulse. A gas bottle equipped with a pressure reducer supplies the fuel. The system was fine-tuned by adjusting a manual valve such that the pressure drop for a given flow rate (measured with a Bronkhorst low-ΔP mass flow meter) was equal. The measurements obtained during the transient are not considered, because the response of the flow meter is relatively slow. The fuel jet and the air stream of the secondary burner were individually seeded with Al_2O_3 particles (nominal diameter 1 μm), supplied by cyclone seeders.

2.2. Solenoid controller and counter

The solenoid valve was controlled by a digital system. A programmable processor (Atmel AVR Mega32) was clocked at a frequency of 10 kHz. Each injection cycle the solenoid counter receives a 24 V DC signal with a duration of approximately 1 s. The solenoid triggering ran independently of the timing of the PIV and PLIF systems. The cycle time was 3.211 s, such that it was not phase-locked with the combined PIV and OH-PLIF measurements that run at 10 Hz: after 10 cycles, measurements are evenly spaced across the cycle-time domain. A 16 bit TTL signal was generated to provide the cycle-time to the measurement devices. This signal was either used directly (in the LDA measurements) or was used as input for a binary LED clock. This device was constructed such that it could be run in continuous or triggered mode thus generating a well-defined time signal in case of longer exposure times of the PIV system.

2.3. Laser Doppler anemometry

A two-component LDA system (manufactured by TSI) was used to measure velocities. The setup is identical to that described in [1]. The external TTL signal of the solenoid controller was connected to the digital input of the TSI system, to obtain velocities measured in time relative to the solenoid pulse.

2.4. CARS temperature measurements

Temperatures were determined with Coherent anti-Stokes Raman Spectroscopy (CARS). The system has been described in detail in [14]. The inaccuracy of the system is estimated at 20 K, and the single-shot imprecision varies from 1% at 2000 K to 4% at 300 K. The weighted fitting procedure, described in [14], was applied to prevent any bias due to temperature gradients. Mean temperatures were determined from 1000 CARS spectra.

2.5. Particle image velocimetry

The measurement setup is outlined in Fig. 2. A high repetition rate Nd:YLF laser (Quantronix DarwinDuo 80-M) was used as a light source for the PIV measurements. The slightly diverging 527 nm beam generated by the laser passed through a positive and two negative lenses, a dichroic mirror (>90% transparency at 527 nm) and through three cylindrical lenses, forming a light sheet of 60 mm height and 0.8 mm thickness. Light scattered by the Al_2O_3 particles was collected through a 200 mm Nikkor ED lens, and recorded by a Photron SA1 high-speed camera. The resulting resolution was around 13 pixels per mm. Both the laser and
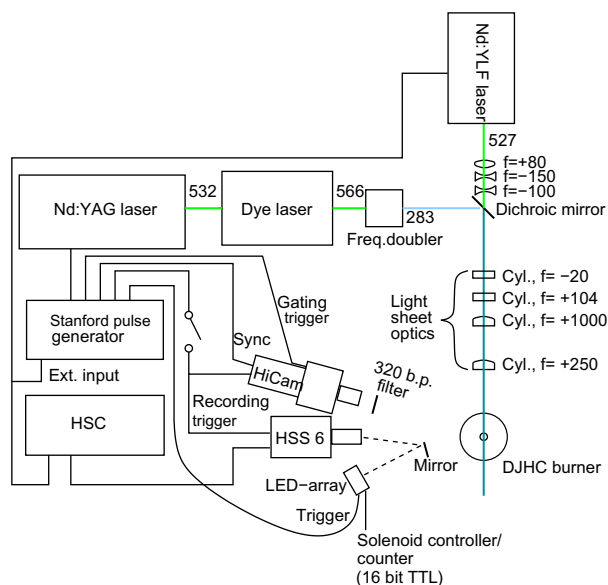
Fig. 2. Schematic overview of the optical and electronic setup for the combined PIV and OH-PLIF measurements.

camera were controlled by a LaVision high-speed controller (HSC). LaVision's software package Davis (version 7.2) was used for the target calibration, data acquisition and the post-processing. Image pairs were captured at either 100 Hz (in conjunction with OH-PLIF measurements) or at 10 kHz. The time between the pulses was set to 20 μs. To determine the relatively low velocities of the coflow the 10 kHz measurements were used, matching the first frames of image pairs k and $k + 2$, resulting in an effective time separation of 200 μs. Processing of the PIV images was done with multiple passes with decreasing interrogation area sizes. To resolve the jet, the interrogation area was 16×16 pixels, for the coflow it was 32×32 pixels. Vectors with peak correlation ratios smaller than 1.4 were rejected. A mirror was positioned at the edge of the field of view such that the binary LED clock could be observed. Cycle times were retrieved in a post-processing step.

2.6. Planar laser-induced OH fluorescence

A Spectra Physics PRO250-10 Nd:YAG laser produced 400 mJ pulses at a wavelength of 532 nm. This beam was used to pump a Syrah PrecisionScan dye laser operating with Rhodamine 590 in methanol. The $Q_1(6)$ line of the $A^2\Sigma^+–X^2\Pi(1,0)$ transition of OH at 282.9 nm was excited, at an energy of 10 mJ/pulse and a repetition rate of 10 Hz. The output beam was transformed into a sheet with a height of 60 mm and a thickness of 0.6 mm, by the same optics as those of the PIV system. Overlapping of the LIF sheet with the PIV sheet was done with the dichroic mirror. The centre-to-centre misalignment of the two light sheets was measured to be less than 0.3 mm. The fluorescence signal was collected through a Semrock narrow pass filter (transmittance exceeding 70% between 300 nm and 320 nm) and a 105 mm Nikkor UV lens, and recorded by a Lambert Instruments HI-CAM CR camera, with a resulting resolution of 11 pixels per mm. The same configuration of lens and camera was also used for the high-speed flame luminescence measurements. Background correction was applied to both the OH-PLIF and the high-speed luminescence images. Additionally, spatial averaging with a disc with a radius of 9 pixels was applied to the high-speed luminescence recordings. Flame structures were recognised from the luminescence images by applying a threshold value of 9, out of a maximum of 255.

2.7. Simultaneous PIV and OH-PLIF measurements

The OH-PLIF measurements were done simultaneously with the PIV measurements. Temporal matching of the PIV and OH-PLIF images enabled timing of the OH-PLIF signal, as the PIV images contained the time data. The trigger pulse of the high-speed controller of the PIV system was used as external timing input for a Stanford DG535 pulse generator, which controlled the Nd:YAG laser and the timing of the intensified camera. The recording of both cameras was triggered with a single external TTL-signal to ensure identical timing. The view direction of the OH-PLIF camera is not perpendicular to the light sheet, but at an angle of 82°. To obtain correctly superimposed PIV and OH-PLIF images, accurate spatial calibrations of both systems are necessary. For the OH-PLIF system, a polynomial fit was calculated, using the pseudo-inverse based on nine reference points of the calibration target. As mentioned before, the calibration routine of the Davis software was used for the PIV images. Due to the high thermal load from the burner to the environment, the position of the optics changed slightly when the burner was operational, leading to deviations between the PIV and OH-PLIF images compared to the cold situation. Therefore, an additional hot-target calibration was performed. For this purpose a stainless steel target, fitting tightly in the fuel tube, was constructed. The target was marked at 10 mm height intervals. After insertion of the target, snapshots with the PIV and OH-PLIF cameras were made, providing the needed translation to match the approximate centre-coordinate, $(r,z) = (0,80)$, of the images. The relative calibration inaccuracy for the superimposed PIV and OH-PLIF images is estimated (from the marks in the hot-calibration pictures) at approximately 0.2 mm in the region of interest (radially between −20 mm and 20 mm, axially between 60 mm and 100 mm).

2.8. Case description

The properties of the coflow are identical to those of the DJHC-I case, which has been described earlier in [1]. Its characteristics are summarised in Fig. 3. The peak coflow temperature of this case is 1540 K (with a standard deviation of 110 K at $z = 3$ mm, r between 5 and 35 mm). The bulk velocity of the coflow is approximately 4 m/s. The measured oxygen mass fraction (mass-flux averaged, between $r = 2.5$ and $r = 35$ mm) is 7.6%, with an inaccuracy of ±0.2%. The oxygen volume fractions, measured with a flue gas analyser, were converted to mass fractions using the data from equilibrium chemistry calculations. The temperature field of the coflow without the central jet, which is the condition at the moment when fuel injection starts, is displayed in Fig. 4.

Because of the challenging nature of the experiments, only two cases were considered, between which the settings of the fuel injection system were varied. This resulted in different velocity histories at the fuel tube exit. The two cases are thus characterised by a fast and slower increase in velocity and a high and lower maximum velocity (with maximum Reynolds numbers of 8800 and 4100, respectively). These cases are termed "fast" and "slow" in the remainder of this paper. The difference between the cases was achieved by a variation in buffer vessel pressure (0.4 bar for the slow case and 1.0 bar for the fast case) and application of the additional buffer for the slower case, see Fig. 1. The temperature of the fuel at the exit of the nozzle in its steady state has been determined to be around 430 K (slow case) and 360 K (fast case). Steady state fuel temperatures at the jet exit were obtained by comparing the mass flux of the fuel stream (known from the mass flow meters) with the volumetric flux obtained by spatially integrating the LDA data. This was done because of the insufficient quality of the CARS signal in the methane-rich, cold environment
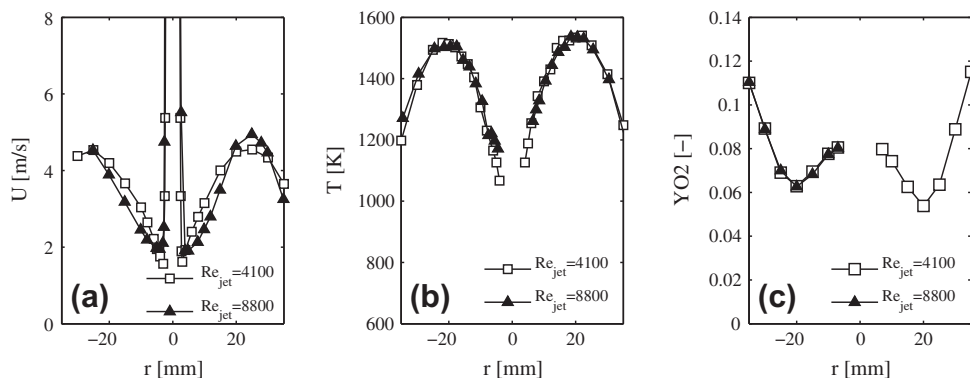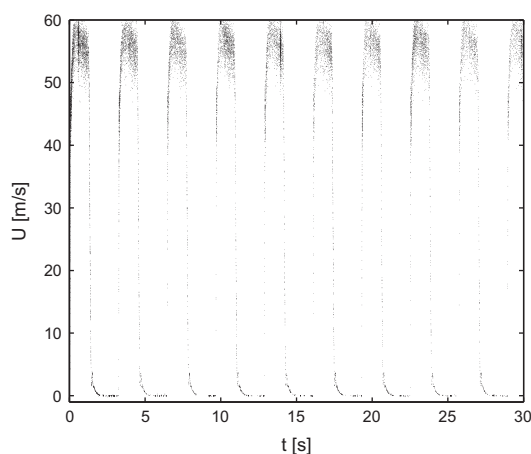
Fig. 3. The boundary conditions at $z = 3$ mm for two steady jet Reynolds numbers: the axial velocity determined with LDA (a), the mean temperature distribution as measured with CARS (b) and the mean oxygen mass fraction measured with a flue gas analyser (c).
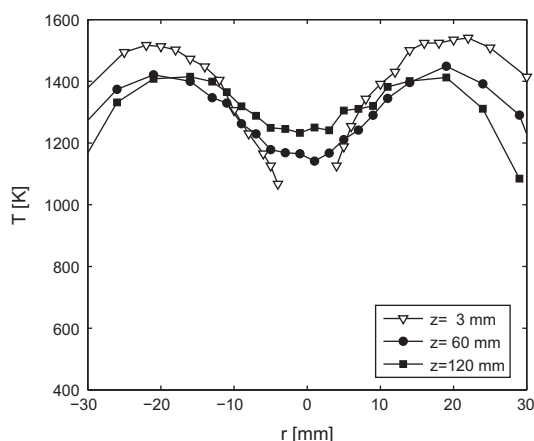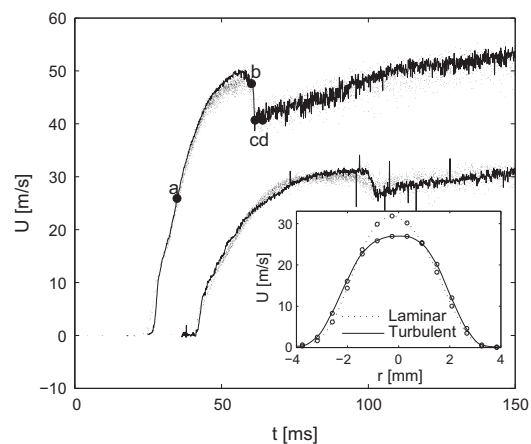

Fig. 4. The mean temperature distribution imposed by the coflow (which forms the situation at $t = 0$) at $z = 3$ mm, 60 mm and 120 mm. The temperatures at $z = 60$ mm and $z = 120$ mm were measured with no jet present. The temperatures at $z = 3$ mm were measured in the presence of the jet, the jet does however not strongly influence the coflow temperature at $z = 3$ mm. In the latter traverse, the jet region is omitted from the figure.

Fig. 5. The axial velocity at $r = 0$, $z = 3$ mm during 10 cycles, fast case.
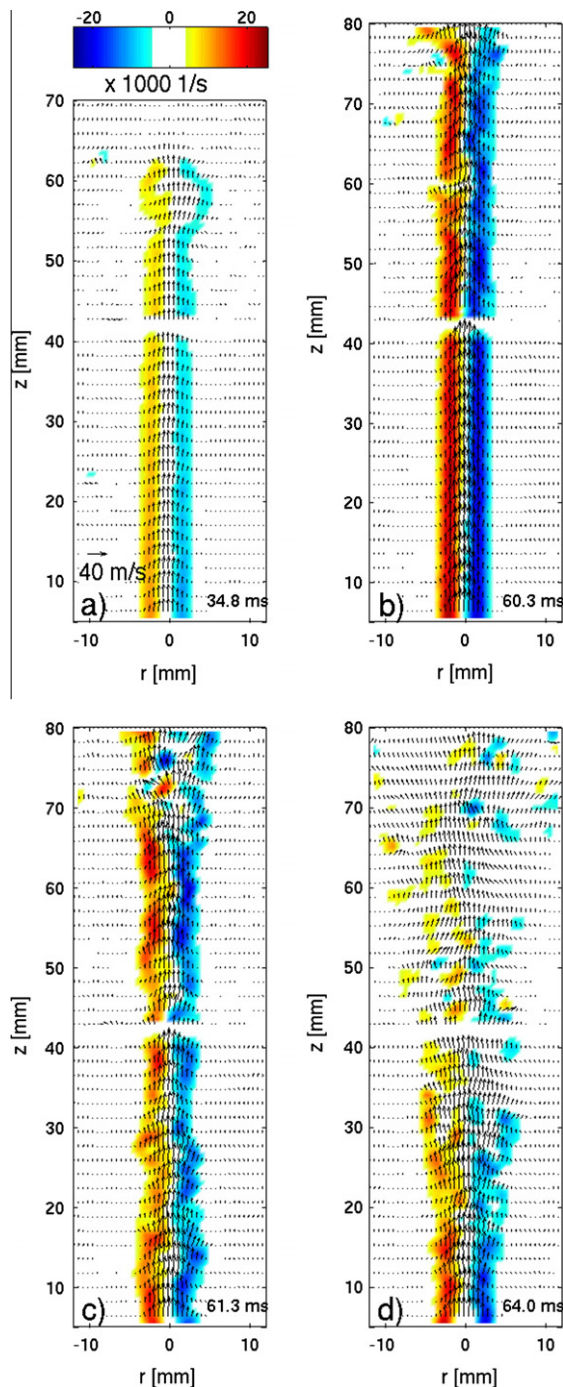

Fig. 6. The axial velocity at $z = 3$ mm from $t = 0$ to 150 ms against cycle time, fast and slow case. The dots are velocities from LDA measurements, spanning 20 cycles. The grey lines are velocities from PIV measurements at 10 kHz. The inset shows average velocity profiles (averaged over 10 frames), 2 ms before ("Laminar") and 2 ms after ("Turbulent") the transition (slow case).

just above the fuel tube exit. The relative accuracy of the temperature, based on inaccuracies of the mass flow meter, LDA statistics and the traversing system, is approximately 6%. The magnitude of the temperature fluctuations cannot be determined with this technique.

When modelling the transient problems described in this paper, the specification of appropriate boundary conditions is challenging. The availability of time-dependent boundary conditions or of boundary conditions at a location so far upstream that the boundary conditions are unaffected by the transient jet would be desirable. Measuring a full (species, temperature, velocity) and time-resolved data set of boundary conditions was not possible with the available techniques. The boundary conditions at $z = 3$ mm are not completely unaffected by the jet velocity, as for instance the lateral velocity of the coflow increases by 0.3 m/s at $r = 15$ mm at an axial height as low as $z = 3$ mm. However, as the scalar properties do not change strongly at $z = 3$ mm as a function of jet Reynolds number (as was shown in Fig. 3), application of the measured boundary conditions at $z = 3$ mm as constant boundary conditions does not seem unreasonable. Alternatively, the boundary conditions might be specified somewhat more downstream (for instance at the burner tube exit at $z = -12$ mm) thereby allowing the lateral velocity to develop. Then, it should be checked that the conditions in the steady state at $z = 3$ mm correspond to those measured.

3. The velocity field

3.1. Axial velocity at the jet exit

LDA was used to measure the axial velocity just above the exit of the fuel pipe (at $r = 0$, $z = 3$ mm). Figure 5 shows the velocity for

sharp rise in velocity with very small scatter. The jet is still laminar during this phase. The reproducibility of the measurements is seen to be very good as the points lie on a thin line in this regime. The data from the time-resolved PIV measurements at 10 kHz are also shown in Fig. 6. These indicate good agreement between the two measurement techniques.
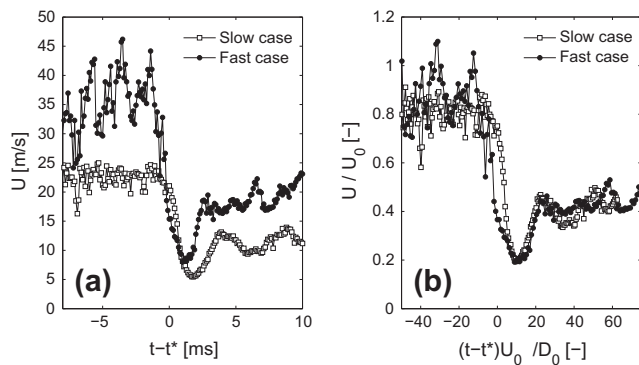
In the fast case, turbulence sets in suddenly, leading to a steep drop in velocity. The drop is not due to a sudden change in volume flux but due to a change in the shape of the velocity profile as illustrated in the inset of Fig. 6. In the case with slow start up, a more gradual transition is seen. Further evidence regarding this transition obtained from the planar PIV measurements is shown in Fig. 7. Given the dimensions of the pipe and the properties of the gas mixture at the inlet temperature, the bulk velocity at a critical Reynolds number of 2300 is approximately 7 m/s. However, as the fuel warms up in the tube as it travels up, its properties change. With fuel at a temperature of 430 K, the critical bulk velocity is roughly 14 m/s. For Poiseuille flow, this corresponds to a centreline velocity of 28 m/s. It is seen in Fig. 6, that the slow case undergoes the transition to turbulence close to that velocity, whereas the fast case has a strong overshoot. This overshoot is related to the stagnant phases in between the fuel injections. During these periods, the jet fuel is subjected to the higher temperatures inside the fuel tube. The heating up of this stagnant volume of fuel has a delaying effect on the laminar-turbulent transition, because of the further increase of kinematic viscosity with temperature. The temperature of the fuel tube in absence of fuel flow has been determined with thermocouple measurements to be approximately 500 K for the lower 0.6 m of its 0.7 m length, but it reaches 820 K in the upper 0.06 m, where the cooling air does not reach the fuel pipe. Considering the characteristic time for conduction of heat into the stagnant gas, r^2/α (with r the tube radius and α the thermal diffusivity of the fuel), of approximately 0.2 s, the fuel will have assumed a temperature close to that of the fuel tube in the stagnant phase. At a temperature of 500 K, the laminar centreline velocity at which the critical Reynolds number is achieved is 40 m/s.

Given the absence of the cooling effect of fuel flow in the stagnant phase, one might also expect the fuel tube to increase in temperature. The heat flux carried away from the fuel tube by the fuel during steady flow is however relatively small. Taking into account its heat capacity, the fuel tube itself is estimated to warm up no more than 15 K in the time the fuel flow is absent. By time-integration of the velocity at the jet exit, it is seen that in both cases the total ejected volume until the moment of the transition approximates the stagnant volume. The transition is therefore expected to be not only caused by an increasing velocity, but also by a rapid change in kinematic viscosity, dropping by an estimated 45% (fast case) and 25% (slow case) to its steady value.

After the transition, the jet still accelerates slightly in both cases due to a gradual increase in pressure. This is caused by the volume present in the system downstream of the solenoid valve, mainly in the cyclone seeder. At $t = 300$ ms, the jet exit velocity reaches its peak value, 33 m/s for the slow case and 58 m/s for the fast case.

3.2. Development of the jet

Rapid events in the flow field can be resolved in time when the PIV system is operated at 10 kHz. The succession of events that takes place after triggering the solenoid valve, and eventually leads to a developed turbulent jet, will be discussed in this section. The timing of these events has been indicated in Fig. 6, for the fast case. The characters a–d in this figure correspond to the subfigures in Fig. 7. At the moment the velocity starts to increase at the jet exit,

Fig. 7. Instantaneous velocity fields for the fast case. The colour scale indicates the magnitude of vorticity. The vertical resolution of the vector grid has been decreased by a factor of three for visual purposes. The upper and lower parts of each of the four subfigures are taken from different runs at identical times after the solenoid valve trigger. (For interpretation of the references to colour in this figure legend, the reader is referred to the web version of this article.)

the fast case, over the course of 10 cycles. In each cycle the jet velocity drops to zero during an interval of approximately 1.5 s. This amounts to approximately fifty times the coflow advection time (with a coflow velocity of 4 m/s and a height of 120 mm) which is sufficiently long for the velocity field to return to its stationary state without the jet. Figure 6 zooms in on the first 150 ms of the cycle, showing data from approximately 20 cycles. During the first 25 ms (fast case) or 41 ms (slow case), there is no response and the velocity remains zero. For both cases, this is followed by a

Fig. 8. The drop in axial velocity on the centreline after the transition to a turbulent state, from the PIV measurements at 10 kHz at $z/D = 16$ (obtained by averaging the vectors between $z = 66$ and $z = 78$ mm). The right plot shows the results with the time axis normalised by the jet time scale, and the velocity axis with the jet velocity. The velocity in the centre of the jet nozzle just after the transition is taken as characteristic jet velocity.

a "mushroom"-shaped vortical structure is formed just above the nozzle.[1] These structures are commonly observed in starting jets [6–9,15,16]. As the lobes of the "mushroom" encounter the relatively slow coflow, long thin structures with a high seeding density are created on either side of the jet. The velocity field near the tip of the starting jet is shown in Fig. 7a. The laminar jet propagates upward with minimal spreading. As the jet accelerates and the Reynolds number increases, flow instabilities start to occur. Initially, the jet is stable at the bottom, but unstable at a height of around 60 mm, fluctuating in position but remaining thin. This is depicted in Fig. 7b. At a certain moment, the flow in the pipe becomes turbulent, leading to the emergence of turbulent structures at the fuel jet exit (Fig. 7c). At the jet exit, the velocity profile suddenly switches from that of a laminar pipe flow to that typical for a turbulent pipe flow: the velocity decreases in the centre and increases somewhat near the edges. This results in a rapid drop in centreline velocity (see also Fig. 6, from b to c). At heights above 30 mm, this sudden transition is accompanied by an instantaneous decrease in the density of the jet seeding, evidence of the strong mixing in the turbulent regime. The slow case also exhibits this transition from laminar to turbulent, although the sequence of events takes place more gradually.

The times of transition to turbulence (defined to lie midway between the time of the fast decay of the velocity in the centre of the nozzle and the time when the velocity in the centre of the nozzle reaches its turbulent value, see points "b" and "c" in Fig. 6) are 61 ms for the fast case and 103 ms for the slow case. The reproducibility of this transition time is estimated at ±0.5 ms for the fast case, and ±1.0 ms for the slow case. Within a time span of a few milliseconds, the unstable jet evolves to a fully turbulent state as the turbulent structures from the jet exit are convected downstream rapidly (Fig. 7d). The centreline velocity inside the considered domain indeed approaches its steady state turbulent value quickly, as shown in Fig. 8a. When the time and velocity axes are rescaled, it is seen that in both cases the centreline velocity reaches its steady state value (of $U/U_0 \approx 0.45$ at $z/D = 16$, [1]) after about 25 integral jet time scales, Fig. 8b. This value cannot be directly compared to the correlations of jet penetration theory, as jet penetration is usually defined using jet fluid mass fractions and applies to axial distances exceeding 20 nozzle diameters [7]. Nonetheless,

it is interesting to note that the time delay is of a similar order of magnitude as predicted by that theory (32 jet time scales at $x/D = 16$).

The initial laminar phase is rather specific for a laboratory set-up, with lower Reynolds numbers than those found in industrial setups. The laminar jet however hardly interacts with the coflow, and the sudden transition toward a turbulent state occurs when the mass flux through the jet is close to its steady value. In this respect, a highly impulsive transient is generated. There is a noteworthy difference between the transient generated here and the transient studied in Fast et al. [11]. In the latter experiments the initially injected fluid was N_2, allowing the jet to develop first, after which the switch from N_2 to DME was made. By doing so, the transient response of the velocity field was decoupled from the injection of DME, allowing specific focus on the chemistry and mixing time scales. In the current study, the effect of the response of the flow field to the transient jet is however also included.

4. Ignition sequence

Now that the sequence of events in the flow field during a cycle has been mapped, ignition events can be related to the flow field. To study ignition events the flame luminescence was monitored with the intensified high-speed camera at 1 kHz such that a useful statistical ensemble, resolving the ignition stage, could be obtained. Ten ignition sequences were recorded for both cases. The data processing (background subtraction, spatial filtering and boundary detection) was done as described in [12]. The flame luminescence was sampled each millisecond, as was the LED light indicating that the solenoid was triggered, resulting in an absolute timing uncertainty of 1 ms. With a sample size of 10, this amounts to a 95% confidence interval for the mean ignition delay due to the limited resolution of the timing of ±0.3 ms. Thus, the reproducibility of the transition itself is normative. Results are presented in Fig. 9. The graytone indicates the presence of flame pockets as a function of height z and cycle time t. For instance, a graytone of value 0.5 indicates that in five out of 10 realisations, a flame structure was recognised at that time at that axial height.
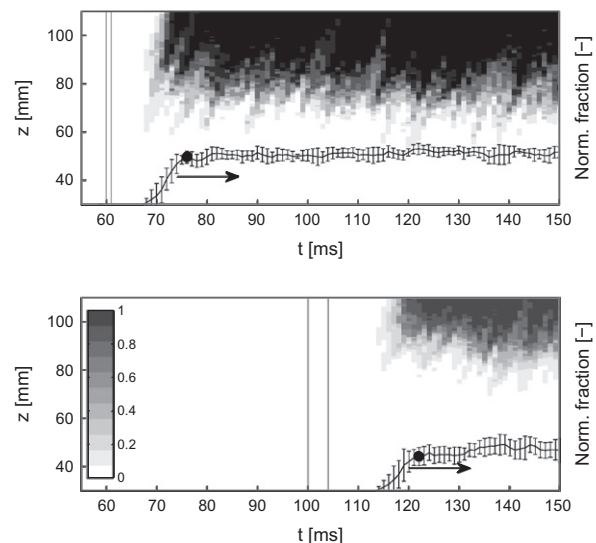
Fig. 9. Ensemble-averaged ignition sequence for the fast (top) and slow (bottom) cases. The grayscale levels indicate the fraction of the realisations that have flame structures present, as a function of axial height z and time t. The lines corresponding to the right axes indicate the (arbitrarily scaled) vertically integrated value. The errorbars have a length equal to the variation of these values between the realisations (standard deviation of the ensemble). The two vertical lines indicate the times of the start of the rapid decay and the steady turbulent state of the velocity at the jet nozzle (Fig. 6, points b and c).

---

[1] Supplementary material available, showing the flow field at the lower ($z = 4$–40 mm) and upper ($z = 45$–80 mm) half of the domain, from two different runs, visualised by the deliberately strongly seeded jet. The LED clock, supplying the cycle times to the PIV frames as explained in Section 2.2, is faintly visible. The right image shows the ensemble-averaged ignition sequence (see Section 4).

After the jet has become turbulent, the flame structures as they are observed in the steady-state flame, typically at a height of $z = 70$ mm and up, are not present immediately. That the ignition and stabilisation process is delayed is not surprising. Not only will there be some chemical delay, the important process of entrainment of coflow fluid needs a turbulent and developed jet. Nevertheless, in terms of jet time scales, the delay is very long: even though after 25 jet time scales (3 and 4 ms for the slow and fast case, respectively) the jet is turbulent and the centreline velocity has reached its steady value, there is not yet any sign of reactions.

In the fast case, ignition kernels start to appear at $t = 70$ ms (9 ms after the transition to turbulence at the jet nozzle) and in the slow case at $t = 117$ ms (14 ms after the transition to turbulence). The standard deviation of the time of their first appearance is approximately 2 ms, larger than the reproducibility of the transition times and the sampling interval of the luminescence but the sample size is too small to deduce an accurate value of the true rms of the ignition events. The ensemble averaged value of the presence of flame pockets approaches its steady state in both cases somewhat later, making the total delay 15 ms for the fast case and 19 ms for the slow case. The moment that a steady-state situation is reached is indicated by the black dots in the error bar plots in Fig. 9. This steady state time is determined by fitting a two-piece linear spline, and determining the crossing point, as illustrated in Fig. 10. The left point of the first part coincides with t_{ign}, the right point of the second part is $t_{ign} + 40$ ms. The optimal split time can be determined based on minimisation of the vertical gap between the left and the right fit, or on a least squares criterion. For the current data, this yields identical results. When applied to computer generated random data with similar rms values and sample size, a trend break (which is where the expectational value has a discontinuous derivative) could be detected with an accuracy of 0.1 ms, and a 95% confidence interval of ±1.1 ms. It is important to note that the gradual transition from first ignition to the steady state situation over several milliseconds is a property of the individual ignition events, and is not due to statistical scatter of individually instantaneous transitions. The timing of the flow- and ignition events is summarised in Table 1.

In the slow case, the first signs of flame structures appear before the transition from laminar flow to turbulent flow. Straight contours of faint luminescence (not recognised by the image processing routine) are seen now and then at $t \approx 90$ ms, at a height of around $z = 100$ mm and up. This kind of flame is also seen when a steady laminar fuel flow is injected. The flame structures are long, and have a relatively stationary but very faint boundary at their trailing edge, unlike the "flame pockets" encountered when the fuel flow is turbulent. With the simultaneous PIV and OH-PLIF measurements, these flame structures are observed more clearly.

Table 1

Summary of flow- and ignition events, expressed in times relative to the solenoid valve trigger. The values between brackets for t_{ign} indicate the 95% confidence interval for the mean (estimated with the t-distribution). The values between brackets for t_{steady} indicate the 95% confidence interval for the technique of applying linear splines as outlined in Fig. 10, determined by applying it to similar computer generated data

Case	t_{trans} (ms)	t_{ign} (ms)	t_{steady} (ms)
Fast	61.0 [±0.5]	69.9 [±1.0]	75.1 [±1.1]
Slow	103.0 [±1.0]	117.0 [±1.6]	121.6 [±1.1]
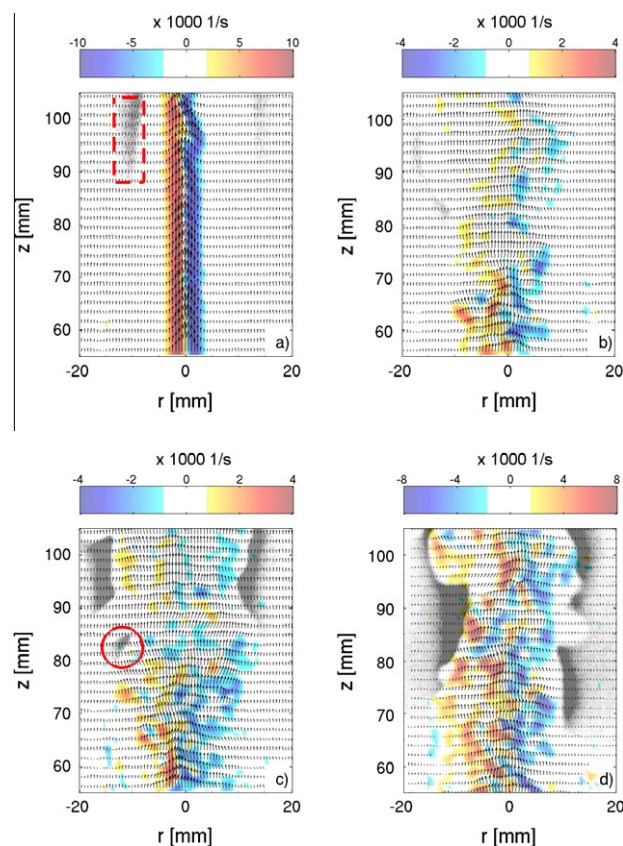
Fig. 11. Four simultaneous PIV/OH-LIF snapshots, (a–c) from the slow case, (d) the fast case. Vorticity contours transparently plotted on OH-PLIF images, the colour-bars corresponding to the vorticity contours are displayed on top. Velocity vectors are again vertically reduced by a factor of 3. (a): Faint flame contour in the slow case $t = 93.4$ ms. (b): Turbulent jet, 12 ms after transition, slow case $t = 115.4$ ms. (c): Slow case, steady state. Note the small encircled flame pocket at $(r,z) = (-12, 84)$. (d): Fast case, steady state. (For interpretation of the references to colour in this figure legend, the reader is referred to the web version of this article.)
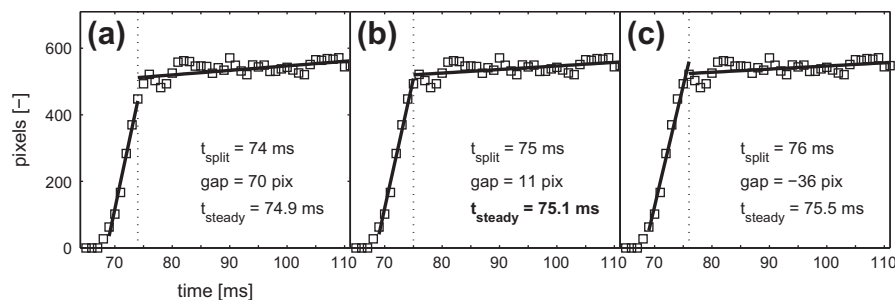
Fig. 10. The procedure by which the time at which a steady burning state is reached is determined, shown for the fast case. (a–c) The trial split between the rising edge and the steady-state is made at $t = 74$ ms, 75 ms and 76 ms, respectively. The gap between the two linear fits left and right of the split is smallest in Fig. 10b. The division at $t = 75$ ms is therefore chosen, and the time when a steady state is reached is determined from the crossing point between the two fits, at $t_{steady} = 75.1$ ms.

Figure 11a shows such a faint flame, enclosed in the dashed box, 10 ms before the transition towards turbulence, around a jet that is still laminar at the bottom but somewhat unstable higher up. The flame structure seems to be the product of a steady autoignition process: a steady stream of fuel/coflow mixture is formed in the low-velocity coflow, ready to ignite at some downstream location that changes only slowly in time. Its maximum radial thickness, judged from the OH-PLIF image, is 3.5 mm. To study the velocity field in the neighbourhood of the flame, the PIV data was first convoluted with a 2-D Gaussian kernel with a width of 1.5 times the vector separation ($\sigma = 0.9$ mm, thus much smaller than the flame thickness) to reduce noise, after which the spatial derivatives were calculated. In the region where the flame is seen in Fig. 11a the velocity field is virtually free from vorticity (the spatially averaged vorticity is 80 s^{-1}), in agreement with the undisturbed appearance of these flame structures. The absolute value of the principle strains is lower than 120 s^{-1}. At the same radial and axial distance at the right side, where no flame is seen, similar values are found. Compared to strain rate values at extinction events measured in flames with non-preheated reactants (1500 s^{-1} [17] or even an order of magnitude higher [18]) this is very low, whereas the preheating typically increases the extinction strain rate, or makes the conventional sharp extinction limit disappear altogether [19]. Given this result, their appearance and disappearance is likely not related to the action of strains imposed by the turbulent field (low strains enabling their ignition or high strains promoting their extinction), but to temporal variations in coflow temperature or in the large-scale convection and diffusion processes that bring the jet fuel and hot coflow together, influencing the sensitive process of auto-ignition.

Figure 11b shows the situation some 20 ms later, 12 ms after the transition to turbulence. No clear sign of any reaction is seen, consistent with the flame luminescence observations. A snapshot of the steady state situation of the slow case is depicted in Fig. 11c. A small flame pocket is encircled, at $(r, z) = (-12$ mm, 84 mm), likely ignited shortly before. The steady state of the fast case, shown in Fig. 11d, shows reactions taking place at lower heights. Note the disconnected reaction zone on the right. In the turbulent cases, the flames also reside in portions of the flow with low vorticity and low axial velocities, typically around 5 m/s. This is in agreement with the convective velocities of the flame pockets determined earlier, obtained by analysing high-speed flame luminescence recordings [12].

Two different time intervals related to the ignition process were examined, namely an ignition delay t_{ign} and a time interval until a steady state is reached t_{steady}. There are at least two reasonable hypotheses on the origin of these delays.

One possibility is that the delay is mainly due to chemical time scales. In that case, the properties of the scalar field are identical to those in the developed turbulent situation. Reactive mixtures are then immediately present, and the time between transition and ignition is the ignition delay of the most reactive mixture. This was the nature of the delay as observed in the experiments reported in [11], where ignition delays were not significantly influenced by jet velocities. Additionally, the turbulent mixing time could be involved, determining how fast homogeneous mixtures of favourable scalar properties are formed. A comprehensive review on this subject can be found in [20].

The second possibility is that the timescales are related to the development of the entrainment process. This seems plausible, given the important role of entrainment on the flame stabilisation due to the radial temperature gradient in the coflow [1]. In this case the scalar field is *not* that of the steady-state turbulent situation, but it has to develop first. The dynamics of this large scale entrainment process are elaborated on in the next section.

5. Transition to turbulent entrainment

The common meaning of "entrainment" when applied to turbulent jets is the process in which irrotational fluid surrounding the jet becomes turbulent. In fluids with Schmidt numbers close to unity, the material interface lies close to the fluctuating vorticity interface [21]. This implies that, as soon as coflow material becomes part of the turbulent jet, it mixes rapidly with the jet fluid. The temperature gradient of the coflow adds an extra dimension to the problem. For the hotter part of the coflow from larger radii to be entrained by the jet, it has to be transported radially inwards first. The rate of entrainment strongly influences the axial height where reactions begin to occur, in an opposite manner as observed in normal lifted flames: higher jet velocities result in lower heights of first reactions and lower lift-off height [1]. The evolution of the entrainment of hot coflow toward the mixing layer is therefore of critical importance.

Although the temperature field has not been measured in a time resolved manner, the transport of temperature can be investigated using the PIV data. Because the turbulent fluctuations of temperature and velocity in the coflow are small compared to their mean values, the heat of the coflow is transported approximately passively [1]. A fluid parcel found somewhere in the coflow therefore still carries information on the temperature from its "injection" (or labelling) point (where it is assumed to be given as a boundary condition), which can be traced back through its pathline.

Because of the nature of the problem, a Lagrangian viewpoint is most natural. Using the notation of Bennett [22], the position of a Lagrangian particle at time t, labeled with its position $\mathbf{x_0}$ at time s is denoted with $\mathbf{x}(\mathbf{x_0}, s|t)$. The streakline $\mathcal{S}(\mathbf{x_0}, t)$ is now defined as the set of locations reached by Lagrangian particles that were labeled at point $\mathbf{x_0}$ in some finite time interval: $t_0 \leqslant s \leqslant t$. In a stationary situation, a streakline $\mathcal{S}(\mathbf{x_0})$ is aligned with the streamline through $\mathbf{x_0}$. In an unsteady situation, this will not be the case. Unlike streamlines, fluid particles need to get convected by the velocity field itself.

If the flow field switches instantaneously from one stationary state to another, the evolution of the streaklines can be expressed explicitly. To this end, define the streakline at $t < t^*$, where t^* is the moment of transition to turbulence, as $\mathcal{S}_L$ (omitting the dependence on time and labelling point for brevity). The streakline at $t > t^*$ is the locus of points belonging to two different sets, one originating from $\mathcal{S}_L$ and one originating from $\mathbf{x_0}$, after the transition:

$$\mathcal{S}(\mathbf{x_0}, t) = \{\mathbf{x}(\mathcal{S}_L, t^* \mid t) \cup \mathbf{x}(\mathbf{x_0}, t^* \leqslant r \leqslant t \mid t)\}, \qquad (1)$$

with $s < t^* < t$.

Therefore, even when the transition of the velocity field is instantaneous, it will take a certain time for the streaklines to reach their steady state. This time is needed to transport the fluid particles pertaining to the old situation $\mathcal{S}_L$ out of the considered domain, and is therefore equal to the ratio of the domain size and the convective velocity in the corresponding direction.

The evolution of the streaklines in the coflow for the fast case is demonstrated in Fig. 12, by the red dots. These dots represent virtual fluid particles, that were injected each frame (0.1 ms separation), starting from $t_0 = -9$ ms, relative to the transition time, with a simple forward integration scheme of the interpolated PIV fields.[2] The streak- and streamlines are clearly aligned initially, detach at the time of the laminar-turbulence transition and realign again, as qualitatively described by Eq. (1). The in-plane velocity component cannot be measured with the 2-D PIV-system. Due to axisymmetry of the flow the tangential velocity component is how-

---

[2] Supplementary material available, showing the development of the stream- and streaklines in an animation.
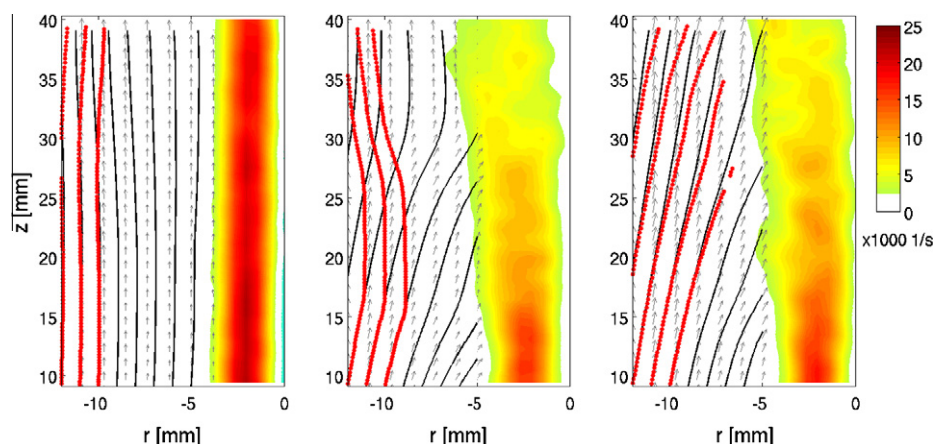
Fig. 12. Streamlines (black lines) and Lagrangian particles (red dots), injected in the coflow starting 9 ms before the transition to turbulence, fast case. Left: 1 ms before transition to turbulence (jet still laminar), middle: 3.2 ms after the transition, right: 13.0 ms after the transition. The colours indicate the vorticity magnitude, averaged over 21 frames (from −1 to +1 ms, relative to the snapshots). (For interpretation of the references to colour in this figure legend, the reader is referred to the web version of this article.)
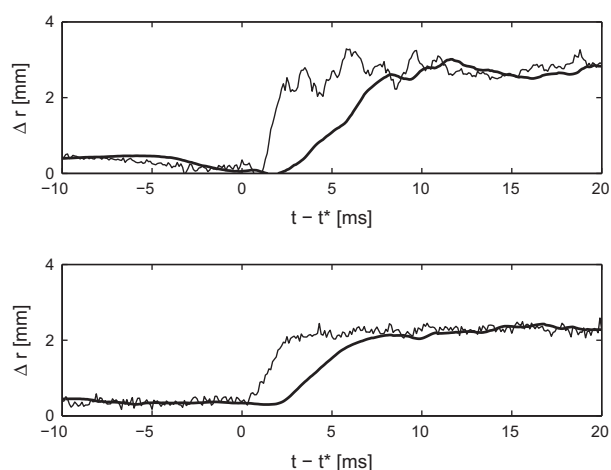
Fig. 13. Radial displacements at $z = 38$ mm of streamlines (thin lines) and streaklines (thick lines) starting at $\mathbf{x_0} = (-14$ mm, 9 mm), fast case (upper) and slow case (lower graph). Time is relative to the start of transition to turbulence.

ever not important to the argumentation. Furthermore, the change in mean radial velocity is more than four times larger than the rms of the radial velocity such that the evolution can be examined from a single realisation.

The response times of both the streaklines and streamlines of the coflow within the field of view of the PIV recordings, which lies roughly between $z = 5$ and $z = 40$ mm, can be quantified using this data. To this end, the radial location of streak- and streamlines that emerge from $\mathbf{x_0} = (-14$ mm, 9 mm) were monitored at an axial height $z = 38$ mm. The resulting values are displayed in Fig. 13. An approximate time until steady-state of the streaklines is in both cases 8 ms. Extrapolating this value to the location where the reaction process were first observed by OH-PLIF and high-speed imaging (roughly $z = 60$ mm for the fast case and $z = 70$ mm for the slow case), approximate delays to the steady state of 12 ms and 14 ms (fast and slow case, respectively) are expected. Keeping in mind that mixing and ignition processes take additional time, these values are in line with the observed values of 14 ms and 19 ms.

The time needed for the streaklines to realign with the vector field is thus of great influence for the delay, but the response time of the vector field itself can not be neglected either. The response of the velocity field surrounding the jet is much faster than that reported in the experiments of Cossali et al. [9]. Interestingly, the

time scales for the response of the vector field and the scalar field in the coflow have different origins. As discussed in Section 1, the adaptation of the vector field is governed by jet time scales. From Fig. 12 it is however evident that the coflow velocity determines how fast the scalar field reaches its steady state. For transient flames, igniting in inhomogeneous surroundings, these two time scales are therefore of relevance. When this insight is applied to furnaces, this means that when large scale inhomogeneities are present, the non-stationary situation might be of a duration multiple times longer than that expected on the basis of jet time scales.

6. Conclusions

Time resolved flow- and ignition processes in the near field ($z/D < 22$) of transient jets of natural gas in a hot coflow were studied, using LDA, PIV, combined PIV/OH-PLIF and flame luminescence. The electronic control system yielded reproducible velocities, such that results from the different measurement techniques could be combined to form a coherent picture of the observed events. Two cases were considered, differing in jet acceleration and velocity, hence their labels "slow" and "fast".

A specific fluid dynamic behaviour, characterised by an initial laminar phase followed by a sudden transition toward a turbulent phase, was observed in both cases. No significant amount of combustion took place during the initial laminar phase. After the transition to turbulence, the velocity field adapted itself relatively fast in both cases (in 3 ms and 4 ms, or around 25 jet time scales), but significant additional delays until ignition and steady state combustion were observed. The average delay times to ignition were 9 ms and 14 ms for the fast and the slow case, respectively. A steady combustion was in both cases achieved 5 ms later. Flame structures were seen to reside in regions where the velocity is close to that of the coflow, in correspondence with earlier findings on the convective velocity of the flame pockets.

The ignition delays were shown to be not merely a function of autoignition chemistry, or the response of the velocity field. Whereas the velocities in the surrounding fluid adapt themselves in time scales governed by the jet diameter and jet velocity, the actual transport of the surrounding coflow fluid to the region where reactions take place occurs on a timescale that is equal to the ratio of the axial distance of this region to the nozzle and the coflow velocity. The observed contribution of these (relatively large) time scales to the ignition delay therefore complements earlier findings on ignition delays and fluid dynamic response of transient jets. An

additional variation in coflow temperatures, which could in principle shed more light on the influence of chemistry, was not undertaken. As a change in coflow temperature leads to a change in lift-off height, the role of chemistry is however always coupled with that of the studied transport processes.

Although the present research was conducted on a specific, laboratory-scale setup with relatively small Reynolds numbers, the observed phenomenon seems to be of general nature, and is therefore expected to apply to large-scale setups as well. With respect to regenerative furnaces, one can therefore conclude that transient processes may be significant during a relative large fraction of the cycle time, depending on the presence of large-scale inhomogeneities.

Acknowledgments

Appendix A. Supplementary material

Supplementary data associated with this article can be found, in the online version, at doi:10.1016/j.combustflame.2011.08.001.

References

[1] E. Oldenhof, M.J. Tummers, E.H. van Veen, D.J.E.M. Roekaerts, Combust. Flame (2011), doi:10.1016/j.combustionflame.2010.12.018.
[2] H. Tsuji, A.K. Gupta, T. Hasegawa, M. Katsuki, K. Kishimoto, M. Morita, High Temperature Air Combustion, CRC Press, 2003.
[3] J.A. Wünning, J.G. Wünning, Prog. Energy Combust. Sci. 23 (1) (1997) 81–94.
[4] H. Zhao, N. Ladommatos, Prog. Energy Combust. Sci. 24 (3) (1998) 221–255.
[5] R.D. Reitz, C.J. Rutland, Prog. Energy Combust. Sci. 21 (2) (1995) 173–196.
[6] A. Joshi, W. Schreiber, Exp. Fluids 40 (1) (2006) 156–160.
[7] P. Ouellette, P.G. Hill, J. Fluid Eng. 122 (4) (2000) 743–752.
[8] N. Atassi, J. Boree, G. Charnay, Appl. Sci. Res. 51 (1–2) (1993) 137–142.
[9] G.E. Cossali, A. Coghe, L. Araneo, AIAA J 39 (6) (2001) 1113–1122.
[10] J.D. Naber, D.L. Siebers, S.S. Dijulio, C.K. Westbrook, Combust. Flame 99 (2) (1994) 192–200.
[11] G. Fast, D. Kuhn, A.G. Class, U. Maas, Combust. Flame 156 (1) (2009) 200–213.
[12] E. Oldenhof, M.J. Tummers, E.H. van Veen, D.J.E.M. Roekaerts, Combust. Flame 157 (6) (2010) 1167–1178.
[13] B.B. Dally, A.N. Karpetis, R.S. Barlow, Proc. Combust. Inst. 29 (2002) 1147–1154.
[14] E.H. van Veen, D. Roekaerts, Combust. Sci. Technol. 175 (10) (2003) 1893–1914.
[15] I. Iglesias, M. Vera, A.L. Sanchez, A. Liñán, Phys. Fluids 17 (3) (2005).
[16] R.P. Satti, A.K. Agrawal, Int. J. Heat Fluid Flow 29 (2) (2008) 527–539.
[17] I. Boxx, C. Heeger, R. Gordon, B. Bohm, M. Aigner, A. Dreizler, W. Meier, Proc. Combust. Inst. 32 (2009) 905–912.
[18] J. Hult, U. Meier, W. Meier, A. Harvey, C.F. Kaminski, Proc. Combust. Inst. 30 (2005) 701–709.
[19] D.H. Rowinski, S.B. Pope, Combust. Theor. Model. 15 (2) (2011) 245–266.
[20] E. Mastorakos, Prog. Energy Combust. Sci. 35 (1) (2009) 57–97.
[21] R.W. Bilger, Annu. Rev. Fluid Mech. 21 (1989) 101–135.
[22] A. Bennett, Lagrangian Fluid Dynamics, Cambridge University Press, 2006.